Applied Energy 348 (2023) 121524

Contents lists available at ScienceDirect

Applied Energy

journal homepage: www.elsevier.com/locate/apenergy

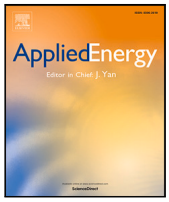

Experimental and numerical investigation of the influence of terrain slope on the performance of single-axis trackers

A. Barbón [a], P. Fortuny Ayuso [b], L. Bayón [b,*], C.A. Silva [c]

[a] Department of Electrical Engineering, University of Oviedo, Spain
[b] Department of Mathematics, University of Oviedo, Spain
[c] Center for Innovation, Technology and Policy Research, Instituto Superior Tecnico, University of Lisbon, Portugal

ARTICLE INFO

Keywords:
Photovoltaic systems
Single-axis trackers
Terrain slope
Mountainous area

ABSTRACT

Certain advantages of using mountainous terrain for the installation of solar plants are well known, such as lower temperature, higher solar irradiance present at high altitudes, and economic aspects related to the lower cost of land. This paper highlights another one: the higher annual solar irradiation incident of single-axis N-S trackers installed on sloping terrain, as compared to horizontal ones. After a theoretical study in which the relevant formulas are derived, numerical simulations are presented. Then we showcase the results of a year-long experiment in which a N-S aligned single-axis tracker prototype was used, at the location of our Department (Gijón, Spain). The experimental results confirm the trends in the formulas and simulations. Finally, theoretical values for the energy gain for different slopes, at locations over the northern hemisphere between latitudes of 6° and 60° are provided. These gains can reach values up to 13.5%.

1. Introduction

After the slight decline due to the COVID-19 pandemic, the global energy demand rebounded strongly in 2021 (by 4.5%) [1]. It is also well known how Oil companies have benefited from the worldwide instability during 2022, which, among other causes was due to the war in Ukraine [2]. Global warming is still one of the main dangers to human society in the mid-term future.

The countries in the European Union (EU) have greatly increased their decarbonization objectives since the Paris agreement in 2015, and this ambition has been revalidated at the United Nations climate change conference in 2021 in Glasgow, Scotland. The updated objectives require the use of renewable energy: solar, wind energy, etc. Remarkably, global solar electricity production in 2020 rose by a record 1.3 (exajoule) (20% increase), whereas wind (1.5 (exajoule)) provided the largest contribution to renewables growth [1]. In 2020, solar capacity expanded by 127 (GW), while wind capacity grew by 111 (GW). The cumulative solar photovoltaic (PV) power generation capacity increased from 23 (GW) in 2009 to 754 (GW) in 2020 [1].

In 2000 the World Conservation Monitoring Centre produced a global map of mountains which defined 24 percent of the Earth's land surface as mountainous [3], using basic criteria such as altitude, slope, and relief. This number gives an idea of the importance of trying to optimize the production of renewable energy in those areas in order to reduce their dependence on fossil fuels [4]. Mountainous areas around the world have some characteristics that may favor the implementation of PV systems:

(i) Temperature effects. Photovoltaic cells are temperature sensitive, and most of the solar energy incident on them turns into heat, which dissipates at a certain rate, depending on the ambient temperature. As a consequence, the module voltage decreases with the ambient temperature, so that its efficiency is higher at low temperatures.
(ii) Solar irradiance. At high altitudes, solar irradiance is more effective [5,6] because there is more beam irradiance and less diffuse, so that PV systems are more efficient.
(iii) Economic aspects. The agriculture sector causes significant increases in land prices, particularly in land-scarce countries in the Middle East, Europe, Japan and Taiwan [7]. The cost of land in the mountainous region is usually cheaper: actually, their price is negatively correlated with the part of the parcel with a slope of more than 15% [8].
(iv) Land use. Land used for agricultural activities has decreased due to the investments in photovoltaic installations [9]. As mountainous land is less useful for agriculture, the impact of PV installations on this will be much less.

The economic aspect and land use are two interrelated issues. To conduct an economic study for the rentability of sloping lands

* Corresponding author.
E-mail address: bayon@uniovi.es (L. Bayón).

https://doi.org/10.1016/j.apenergy.2023.121524
Received 28 March 2023; Received in revised form 25 May 2023; Accepted 24 June 2023
Available online 10 July 2023

Nomenclature

A	Longitudinal tilt angle (°)
EG	Energy gain (%)
H_t	Total irradiation on a tilted surface (Wh/m^2)
I_{bh}	Beam irradiance on a horizontal surface (W/m^2)
I_{dh}	Diffuse irradiance on a horizontal surface (W/m^2)
I_t	Total irradiance on a tilted surface (W/m^2)
n	Ordinal of the day (day)
$\overline{n}_S$	Solar vector
T	Solar time (h)
T_R	Sunrise solar time (h)
T_S	Sunset solar time (h)
β	Tilt angle of photovoltaic module (rad)
β^A	Rotation angle of the tracker (°)
γ	Azimuth angle of photovoltaic module (°)
γ_s	Azimuth of the Sun (°)
δ	Solar declination (°)
θ	Incidence angle (°)
θ_B	Incidence angle in the backtracking mode (°)
θ_{NT}	Incidence angle in the normal tracking mode (°)
θ_S	Incidence angle in the global reference system (°)
θ_t	Classical solar transversal angle relative to a horizontal surface (°)
θ_t^A	Solar transversal angle (°)
θ_z	Zenith angle of the Sun (°)
λ	Latitude angle (°)
ρ_g	Ground reflectance (dimensionless)
ω	Hour angle (°)

compared to flat lands at higher latitudes, several factors need to be considered. These factors include: (i) land cost, (ii) land productivity, (ii) topography, (iii) climate, and (iv) access to markets. How these factors may affect the profitability of sloping land compared to flat land at higher latitudes will be discussed below:

(i) Land cost. In general, sloping lands are cheaper than flat lands because they are more difficult to farm and develop. However, the exact cost of the land will depend on its location, soil quality, and other factors.

(ii) Land productivity. Sloping lands tend to be less productive than flat lands because they have less soil depth and water retention capacity [10]. There are several studies that corroborate this fact. In olive orchards, the value of net return and benefit to cost ratio indicated that olive production is more economical in flat orchards [11] . Land with slopes steeper than 10% tends to have the highest percentage of very low quality soils [12]. In addition, the land with steep slopes can also be difficult to cultivate effectively with the large machinery typical of modern agricultural production. However, if managed properly, sloping lands can still be productive and can even offer some advantages over flat lands. For example, sloping lands can be used for terracing, which can increase the effective growing area and reduce erosion [13].

(iii) Topography. Sloping lands can be more challenging to farm than flat lands because of the slope gradient and the need for terracing [14]. This can increase labor costs and reduce the amount of land that can be cultivated. In contrast, flat lands are easier to farm and require less labor [15].

(iv) Climate. The climate of the region where the land is located can also have a significant impact on its rentability. For example, in colder regions, flat lands may be more suitable for agriculture because they warm up faster in the spring and can be planted earlier in the season [16].

(v) Access to markets. The rentability of the land will also depend on its proximity to markets and transportation infrastructure [17]. If the land is far from markets, transportation costs may be higher, reducing its rentability.

Table 1
Ratio of energy loss with respect to the dual-axis tracker.

Racking system	Maximum loss of energy	
	Latitude < 45 (°)	Latitude > 45 (°)
Polar-axis tracker	3.46%	4.65%
North–South aligned axis tracker	11.15%	15.88%
East-West aligned axis tracker	21.95%	19.45%
Without solar tracker, with optimum tilt angle	27.82%	24.49%

It can be concluded that the profitability of sloping versus flat land at higher latitudes will depend on site-specific circumstances. In general, sloping lands may be less rentable than flat lands because of their lower productivity and higher labor costs. Ultimately, the decision of whether to invest in sloping lands or flat lands will depend on a careful analysis of the local conditions and the goals of the investor.

However, there are obvious drawbacks associated to PV installations in mountainous lots. First of all, they need a road network [18], and one which makes the implementation and operation and maintenance cost reasonable. They also may be prone to suffer greater environmental impact, as power transmission lines are required. As an example, landscape interventions in national parks is forbidden by Law in the EU [19], for instance.

The usual categorization of racking systems in PV power is: dual-axis and single-axis trackers, and no-tracking systems. Single-axis systems can be deployed with different geometries [20]: (i) horizontal axis with North–South alignment (named “single-axis trackers aligned with the North–South axis”); (ii) horizontal axis with East–West alignment (named “single-axis trackers aligned with the East–West axis”) and (iii) parallel to the Earth’s axis with North–South alignment (named “Polar axis trackers”).

Dual-axis trackers ensure the reception of the maximum beam irradiance possible at all times, and are used as the reference point when studying the efficiency of the other systems. Table 1 summarized the comparison of the other systems with the dual-axis tracker in 39 cities located between 6 (°) and 60 (°) North latitude [20]. However, when studying possible deployments, there are many factors apart from energy efficiency to take into account [20]: initial investment cost, soil condition, topography, expected lifespan, energy consumption during operation, operation and maintenance costs, wind loads...

Martin et al. [21] evaluated six large PV power plants in Spain with different racking systems for several years of operation and concluded that the operation and maintenance costs of dual-axis trackers are underestimated. Several studies [20,22] using the levelized cost of electricity as an indicator, have shown that single-axis trackers are preferable, and as a matter of fact, they are the most commonly deployed [23]. According to a report by Wood Mackenzie company [24], the use of dual-axis trackers is expected to grow at a faster rate than single-axis trackers in the coming years. The report predicts that dual-axis trackers will account for about 10% of the global tracker market by 2025, up from just 1% in 2019. However, single-axis trackers will still account for the majority of solar tracking installations in the

coming years, due to their lower cost and widespread use in utility-scale projects. According to the same Wood Mackenzie report [24], single-axis trackers are expected to account for 90% of the global tracker market by 2025. They will be the only object of study in this paper.

From Table 1 one might conclude that the polar-axis tracker is the best alternative to the dual-axis tracker. However, it has several well-known drawbacks: (i) its ground coverage ratio is low, (ii) it is more complex to install, (iii) it requires more sophisticated control systems, and (iv) it is more sensitive to wind loads. These aspects are further developed below:

(i) The polar-axis tracker has a low ground coverage ratio. The ground coverage ratio (GCR) of a solar tracking system refers to the ratio of the total land area required to install the system, to the area of the PV modules themselves. A lower GCR is desirable, as it means that less land is required to generate a given amount of electricity. In the case of a polar-axis tracker, the GCR is typically lower than that of other types of solar tracking systems [25]. This is because the PV modules are mounted on a single axis that is oriented North–South, and they rotate around this axis to track the Sun throughout the day. This means that the PV modules can be spaced relatively far apart, which reduces the amount of land required to install the system.

(ii) The polar-axis tracker is more complex to install. One reason for this is that polar-axis trackers require a very precise alignment with the Earth's rotational axis, which can be difficult to achieve during installation [23]. This typically involves using specialized tools and techniques to ensure that the tracker is perfectly aligned, such as using a GPS system to locate the exact position of the North Pole.

(iii) The polar-axis tracker requires more sophisticated control systems to adjust the position of the PV modules throughout the day. This typically involves using sensors and software to calculate the position of the Sun and adjust the angle of the PV nodules accordingly [26].

(iv) The polar-axis tracker is more sensitive to wind loads. As one end of the polar-axis tracker is much higher than the other, this type of solar tracker is more sensitive to wind loads [27]. The higher the tracker is, the more wind load it will experience, so in high latitude locations this is a major drawback, which increases the cost of the tracker. Polar-axis trackers usually have a robust and reinforced frame, made of materials such as steel, which helps resist deformation and damage caused by wind forces.

From Table 1 it can be also concluded that the single-axis trackers aligned with the North–South axis is the second best alternative to the dual-axis tracker. Notice that a single-axis tracker installed on a sloped terrain, and aligned with the North–South axis becomes a polar-axis tracker if the terrain slope is equal to the latitude of the installation site [28]. Fig. 1 shows a schematic of these two types of solar trackers. The N-S oriented single-axis tracker has a higher ground coverage rate than the polar-axis tracker, which reduces the overall cost of the project. In terms of installation, the N-S oriented single-axis tracker is much less complex to install than the polar-axis tracker, which lowers the overall cost of the project [23]. The control system of the N-S oriented single axis tracker is less sophisticated than the polar-axis tracker, which also reduces the overall cost of the project [23]. Although wind loads can be an issue for any type of PV plant, as they can be significant in some locations, the high height of the polar-axis tracker compared to the N-S oriented single-axis tracker implies the use of more robust and reinforced frames [23]. For these reasons, the use of N-S oriented single-axis trackers is much more widespread than polar-axis trackers.

Therefore, in this work we study single-axis trackers aligned with the North–South axis on sloped terrain slopes. This allows, on one hand, to take advantage of at least part of the tilt inherent to polar

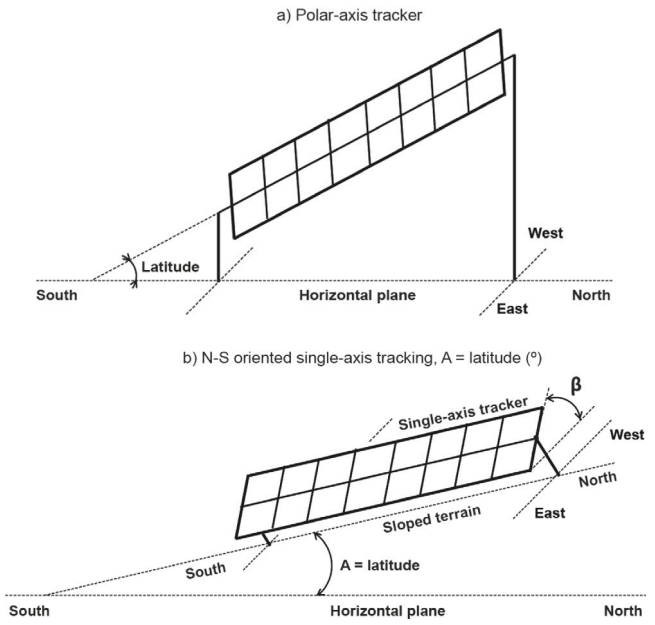

Fig. 1. Schematic of a polar-axis tracker and a single-axis trackers aligned with the North–South axis.

trackers in terms of energy received, and, on the other, to avoid the aforementioned problems of polar trackers. If the aim were to mirror these, the slope of the terrain should equal the latitude of the site. But this is difficult to achieve and may even be unrealistic at some latitudes. Our aim is to assess the efficiency of these systems when the slope of the terrain is different (usually less) to the latitude.

We provide both experimental and theoretical results and estimates. We first present the former, deriving general formulae for any tilt angle A of the terrain in the North–South direction, and we carry out numerical simulations. Formulas for normal tracking and backtracking can be found in the literature for trackers placed on horizontal terrain [29,30].

Generalizing the results briefly presented in [31], general formulas for arrays of N-S oriented trackers built on West-facing slopes have been developed in [32]. The authors describe three backtracking strategies: the "standard one", which is the same as for horizontal surface; one using the same equations but with a ground coverage ratio (GCR) different from the array's true GCR (although it is not clear how to choose the value of this adjusted GCR, and this method seems like an imperfect solution); and a third one which is the slope-aware backtracking routine of [33].

In [33] the authors also study the general case, giving closed-formed equations for the true-tracking angle, the backtracking angle, the shaded fraction and the orientation angles of single-axis trackers on arbitrarily oriented slopes. However, there are several key technical aspects which are missing (probably due to its being a mostly geometric study): the maximum rotation angle of the system, the (real) possibility of having the Sun "behind" the tracker (for instance, on the Summer equinox, at times near the start and end of the working period), and the effective working periods. All these problems are covered in our work, and this is one of the distinguishing factors.

In [34], cross axis slopes (i.e. E-W slopes for tracking systems with a N-S axis) are also studied, with three different backtracking modes (baseline, commissioned, and SmarTrack™). The latter is an innovative control platform by Arrays which includes backtracking optimization for sloped terrain.

However, there is no general solution for terrain with variable, nonuniform slopes. Several commercial packages have been presented recently. For instance, in [35] improvements to SolarFarmer's 3-D tracker shading algorithm are presented. They show that SolarFarmer

can be used to calculate tracker terrain loss (i.e. the difference between the performance of trackers on horizontal ground and that on variable terrain). Similarly, in [36] work by Nevados Engineering is demonstrated, which can handle multiple slopes in any direction, using forward ray tracing and the methodology described in [33].

We then provide another study which is completely absent in the literature: we show the results of the tests we have carried out on a prototype of a single-axis tracker aligned with North–South located at the Electrical Engineering Department of the University of Oviedo (Gijón, Spain), using three pyranometers, each with a different longitudinal tilt angle: 0 (°), latitude/2 (°) and latitude (°). Our research investigation covers a *whole year* of measurements of monthly solar irradiance. Finally, we study the influence of the latitude by means of simulations for different locations around the world.

The paper is organized as follows: the solar tracking geometry is presented in Section 2. Section 3 provides the technical aspects of a N-S orientation single-axis tracking. The annual solar irradiation incident on a single-axis tracker with tilted axis is presented in Section 4. Section 5 contains several numerical simulations. Section 6 describes the experimental setup, including the system description and the measurement equipment. In Section 7 we show the experimental results and their discussion. Section 8 covers the simulations of the influence of the terrain slope on the performance of single-axis trackers around the world. Finally, Section 9 summarizes the main contributions and the conclusions of the paper.

2. Geometry of solar tracking

The orientation of the Sun with respect to a *PV* tracking system throughout the day depends on three angles: the tilt angle of the ground surface on which it is built with respect to the horizontal; the azimuth angle of said surface; and the incidence angle θ of the solar rays. The main studies on proper orientation of solar tracking systems are [37,38], and [33]. However, no thorough theoretical study, with both explicit equations and interpretation of the results for single-axis trackers aligned with the North–South axis installed on sloped terrains exists yet. We provide them in this section, assuming the system is in the Northern Hemisphere.

The solar position can be determined by the solar vector $\overline{n}_S$: a unit vector located at the center of the Earth, pointing to the Sun, which in the global reference system (S) is given by Eq. (1):

$$\overline{n}_S = (\sin\omega\cos\delta, \cos\omega\cos\delta, \sin\delta)\cdot(\overline{i},\overline{j},\overline{k}) \tag{1}$$

where δ is the solar declination (°) and ω is the hour angle (°). In the local system of reference (S') (called also the Earth system), we have

$$\overline{n}_S = (\sin\omega\cos\delta, \cos\omega\cos\delta, \sin\delta)\cdot(\overline{i},\overline{j},\overline{k})$$
$$= (\sin\omega\cos\delta, \cos\omega\cos\delta, \sin\delta)\cdot\begin{pmatrix}1 & 0 & 0\\ 0 & \sin\lambda & \cos\lambda\\ 0 & -\cos\lambda & \sin\lambda\end{pmatrix}\cdot\begin{pmatrix}\overline{i'}\\ \overline{j'}\\ \overline{k'}\end{pmatrix} \tag{2}$$

(where λ is the latitude of the location (°)). Expanding, we obtain:

$$\overline{n}_S = (\sin\omega\cos\delta, \cos\omega\cos\delta\sin\lambda - \sin\delta\cos\lambda, \cos\omega\cos\delta\cos\lambda + \sin\delta\sin\lambda)$$
$$\cdot(\overline{i'},\overline{j'},\overline{k'}) \tag{3}$$

In this local system of reference, the Ox' axis points West, the Oy' axis points South, and the Oz' axis points toward the zenith. Fig. 2 gives an idea of all the geometric elements we shall use.

The slope of the terrain imposes some adjustments to these equations. We shall call A the angle (°) of the axis of the solar tracker with respect to the horizontal (i.e. not to the terrain), and we name it the longitudinal tilt angle. We use the convention $A > 0$ when the normal to the tracker pointing away from the Earth points South, and $A < 0$ otherwise. Consider the system of reference relative to the axis of the tracker (S'') (Ox'', Oy'', Oz'') in Fig. 2, which is obtained by rotating

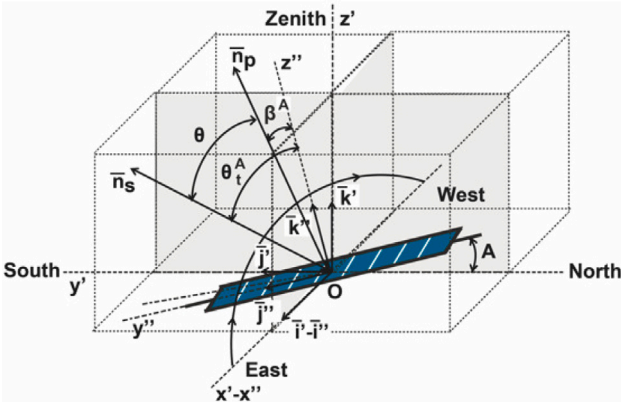

Fig. 2. Solar geometry used in the current study.

(Ox', Oy', Oz') around Ox' by the angle A. The solar vector can be expressed in this new system as:

$$\overline{n}_S = (\sin\omega\cos\delta, \cos\omega\cos\delta\sin\lambda - \sin\delta\cos\lambda, \cos\omega\cos\delta\cos\lambda + \sin\delta\sin\lambda)\cdot$$
$$\cdot\begin{pmatrix}1 & 0 & 0\\ 0 & \cos A & \sin A\\ 0 & -\sin A & \cos A\end{pmatrix}\cdot\begin{pmatrix}\overline{i''}\\ \overline{j''}\\ \overline{k''}\end{pmatrix} \tag{4}$$

which expands to

$$\overline{n}_S = (\sin\omega\cos\delta, \cos\omega\cos\delta\sin(\lambda - A) - \sin\delta\cos(\lambda - A),$$
$$\cos\omega\cos\delta\cos(\lambda - A) + \sin\delta\sin(\lambda - A))\cdot(\overline{i''},\overline{j''},\overline{k''}) \tag{5}$$

The incident angle θ, which is the angle between $\overline{n}_S$ and the normal (pointing away from the Earth) to the surface of the collector $\overline{n}_P$ satisfies:

$$\cos\theta = \frac{\overline{n}_S\cdot\overline{n}_p}{|\overline{n}_S|.|\overline{n}_p|} \tag{6}$$

For the sake of coherence with the classical usage, we shall denote β^A(°) the rotation angle of the tracker, which is the angle between $\overline{n}_p$ and Oz'', and θ_t^A the solar transversal angle (°), which is the angle between $\overline{n}_s$ and Oz''. Notice that both are expressed in the system of reference of the tracker S''. From Eq. (5), we infer:

$$\tan\theta_t^A = \frac{\sin\omega\cos\delta}{\cos\omega\cos\delta\cos(\lambda - A) + \sin\delta\sin(\lambda - A)} \tag{7}$$

Also, we have the following equality involving β^A:

$$\overline{n}_p = (\sin\beta^A, 0, \cos\beta^A)\cdot(\overline{i''},\overline{j''},\overline{k''}) \tag{8}$$

(see Fig. 2), and we obtain one of our main equalities:

$$\cos\theta = \sin\beta^A(\sin\omega\cos\delta) + \cos\beta^A(\cos\omega\cos\delta\cos(\lambda - A) + \sin\delta\sin(\lambda - A)) \tag{9}$$

In order to maximize the beam irradiance collected by the system, the angle β^A must be such that the projection of $\overline{n}_S$ on a plane perpendicular to the collector is parallel to the $\overline{n}_P$. This will be called the optimal pointing condition, and is given by the equation:

$$\beta^A = \theta_t^A = \arctan\left[\frac{\sin\omega\cos\delta}{\cos\omega\cos\delta\cos(\lambda - A) + \sin\delta\sin(\lambda - A)}\right] \tag{10}$$

Sign convention: We shall always set $\beta^A < 0$ before noon and $\beta^A > 0$ after. This is just to match our calculations with the data from the prototype.

We remark that Eq. (10) includes, as particular cases, the clásicas formulas in [37] for North–South Horizontal ($A = 0$) and Polar ($A = \lambda$) systems:

$$(i)\ A = 0 \Rightarrow\ \beta^A = \theta_t \tag{11}$$

$(ii)\ A = \lambda \Rightarrow\ \beta^A = \omega$

where θ_t is the classical solar transversal angle relative to a horizontal surface (°):

$$\theta_t = \arctan(\tan\theta_z \sin\gamma_s) \tag{12}$$

Setting:

$$C_1 = \sin\omega\cos\delta \tag{13}$$
$$C_2 = \cos\omega\cos\delta\cos(\lambda - A) + \sin\delta\sin(\lambda - A)$$

we obtain the equalities:

$$\cos\theta = C_1 \sin\beta^A + C_2\cos\beta^A \tag{14}$$
$$\tan\beta^A = \frac{C_1}{C_2} \rightarrow C_1 = C_2\frac{\sin\beta^A}{\cos\beta^A}$$

which allow us to eliminate β^A:

$$\cos\theta = \frac{C_2}{\frac{C_2}{\sqrt{C_1^2+C_2^2}}} = \sqrt{C_1^2+C_2^2} \tag{15}$$

providing the following formula for the incident angle under optimal pointing (i.e. normal tracking):

$$\cos\theta = \cos\delta\sqrt{\sin^2\omega + (\cos\omega\cos(\lambda - A) + \tan\delta\sin(\lambda - A))^2} \tag{16}$$

As a side note, Eq. (16) includes the formulas in [37] for North–South Horizontal ($A = 0$) and Polar ($A = \lambda$) systems:

$(i)\ A = 0 \Rightarrow\ \cos\theta = \sqrt{\cos^2\theta_z + \cos^2\delta\sin^2\omega}$

$(ii)\ A = \lambda \Rightarrow\ \cos\theta = \cos\delta$

where θ_z is the zenith angle. In later sections, we will only use these two angles β^A and θ in the computations in the irradiance models. However, we have included, in Appendix, the deduction of the formulas for the tilt angle β, and the tracker and azimuth angle γ in the local system of reference (S′). We do this for the sake of completeness and to assist the reader in the comparison between our general formulas and those for horizontal terrains.

3. Technical considerations for N-S oriented single-axis tracking

Recall that we are only studying North–South axis aligned single axis trackers with East–West tracking.

3.1. Operating modes

One can distinguish three different operating modes, according to the position of the Sun, the shadows projected by the system and its rotational limitations. These modes are: backtracking, static, and normal.

3.1.1. Bactracking

During low solar elevation intervals (sunrise and sunset) some *PV* modules may project shadows on others, depending on their rotation. This must be avoided at all costs, and the motion achieving this is called backtracking [39]. The tilt angle is calculated so that no module projects a shadow on any other (namely, the next one) and the beam irradiance is maximal under that condition.

To deduce the backtracking formulas (which is done imposing the condition of no shading), one only needs to cut the system with a plane transverse to the axis of the tracker (see Fig. 3).

When taking into account the terrain slope A, the backtracking formula must take into account the solar transverse angle θ_t^A (°) (in the system of reference of the tracker, S''). Thus, keeping our sign convention, we have:

$$\beta_B^A = \theta_t^A - \text{sign}(\omega)\cdot\arccos\left(\frac{e_t}{W}\cos\theta_t^A\right) \tag{17}$$

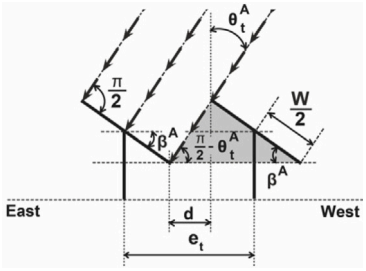

Fig. 3. Detail of the transversal study of the installation.

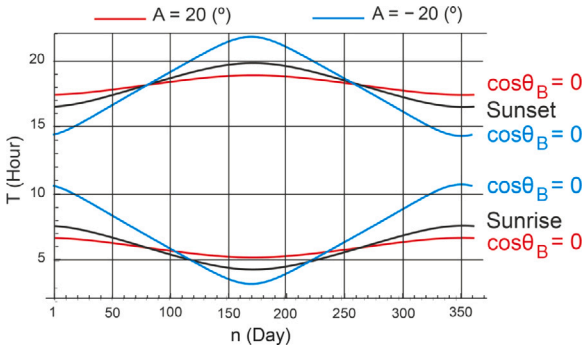

Fig. 4. Influence of backtracking in Gijón.

where W is the width (m) of the mounting system and e_t (the pitch) is the East–West distance (m) between the columns of two adjacent mounting systems. Notice the parallelism between this formula and the classical ones in [29] (in the absence of tilt A, the correction is made on θ_t).

From (9), we obtain:

$$\cos\theta_B = \sin\beta_B^A(\sin\omega\cos\delta) + \cos\beta_B^A(\cos\omega\cos\delta\cos(\lambda - A) + \sin\delta\sin(\lambda - A)) \tag{18}$$

where the subindex B indicates "backtracking" mode.

One of the most relevant consequences of taking A into account is that there may be periods during some days when $\cos\theta_B$ can be negative. This fact, which is well known for static tables, never happens for horizontal trackers, but needs to be taken into account for tilted ones, as the system is ineffective during those periods.

Roughly speaking, when $A > 0$, between day 81 and 265 (the two equinoxes), $\cos\theta_B$ is negative near sunrise and sunset. Fig. 4 shows the case $A = 20$ (°) at the location in Gijón (Spain). For $A < 0$ this phenomenon takes place on the complementary dates (from the autumn equinox to the spring one), as also Fig. 4 shows for $A = -20$ (°) at the same location. The times when this happens need to be known when predicting the daily irradiation, as the tracker receives no irradiation then.

3.1.2. Static mode

Trackers have a limited rotation range, which depends on the manufacturer but is around $\beta_{\max} = 60^o$ [23] (which is the value we will consider in this study). Thus, whenever the theoretical value of the rotation angle β^A is greater than $\beta_{\max}$, one must set it to $\beta_{\max}$:

$$\beta_M^A = \beta_{\max} \tag{19}$$

From (9), with the adequate sign convention, we obtain:

$$\cos\theta_S = \sin\left(\text{sign}(\omega)\beta_M^A\right)(\sin\omega\cos\delta)$$
$$+\cos\left(\text{sign}(\omega)\beta_M^A\right)(\cos\omega\cos\delta\cos(\lambda - A) + \sin\delta\sin(\lambda - A)) \tag{20}$$

where the subindex S is used to indicate the static mode.

Table 2
Operating periods of the solar tracker.

Operating period	Start	End	Tilt angle β^A	Incidence angle
Backtracking	T_R	T_{B_1}	β_B^A	$\cos\theta_B$
Static	T_{B_1}	T_{M_1}	$-\beta_M^A$	$\cos\theta_S$
Normal tracking	T_{M_1}	T_{M_2}	θ_t^A	$\cos\theta_{NT}$
Static	T_{M_2}	T_{B_2}	β_M^A	$\cos\theta_S$
Backtracking	T_{B_2}	T_S	β_B^A	$\cos\theta_B$

3.1.3. Normal tracking mode

The solar trackers under study rotate in order to maximize the cosine of the angle of solar incidence [37]. This is achieved by matching the rotation of the tracker to the projection of the Sun's position onto the plane of rotation of the tracker. This "optimal pointing" condition determines the rotation angle β^A. Instead of using the formula:

$$\beta^A = \arctan\left[\frac{\sin\omega\cos\delta}{\cos\omega\cos\delta\cos(\lambda-A)+\sin\delta\sin(\lambda-A)}\right] \tag{21}$$

one should prefer using the function arctan2, which has as range the whole circumference $(-180^o, 180^o]$:

$$\beta^A = \arctan 2\left[\cos\omega\cos\delta\cos(\lambda-A)+\sin\delta\sin(\lambda-A), \sin\omega\cos\delta\right] \tag{22}$$

When one can rotate by this β^A, formula (16) hold:

$$\cos\theta_{NT} = \cos\delta\sqrt{\sin^2\omega+(\cos\omega\cos(\lambda-A)+\tan\delta\sin(\lambda-A))^2} \tag{23}$$

where the subindex NT denotes the normal tracking mode of operation.

3.2. Operating periods

One needs to determine the periods in which the tracker is in each different mode of operation. This computation is not obvious, as there are many contributing factors: the pitch e_t, the latitude λ of the site, the value of $\beta_{\max}$... In our case, the three modes of operation (backtracking, normal and static) are distributed in five different time ranges, as shown in Table 2. This is the most general case; the reader must take into account that there are in specific installations, the static mode may not occur.

The solar times T (h) corresponding to sunrise $T_R(n)$ and sunset $T_S(n)$ are computed using classical formulas [37] (we call n the day of the year).

Eq. (22) allows finding the endpoints of the timespan $[T_{M_1}(n), T_{M_2}(n)]$ when $\beta^A = \beta_{\max}$.

As regards the computation of the backtracking period, one needs just use Fig. 2 to deduce the relations that follow. For e_t:

$$e_t = \frac{W}{\cos\theta_t^A}\cos(\theta_t^A - \beta^A) \tag{24}$$

For d, setting the rotating the tracker β_M^A, we get:

$$d = e_t - W\cos\beta_M^A \tag{25}$$

And we also have:

$$d = W\tan\theta_t^A\sin\beta_M^A \tag{26}$$

from which one can compute the values of θ_t^A (and hence the endpoints T_{B_1} and T_{B_2}.

The influence of the terrain slope A on the operating periods is shown in Fig. 5. Notice how, for $A > 0$ (°) (see Fig. 5a, which corresponds to $A = 20$ (°) in Gijón (Spain)), the normal tracking period is longer during autumn, winter, and spring, whereas it is shorter in summer, whereas the opposite happens for $A < 0$ (°). Fig. 5b shows the case $A = -20$ (°) also in Gijón. This phenomenon is key to optimize the efficiency of the tracking system.

3.3. Terrain slope

Theoretically, we can set the slope angle A to any value. As we are working in the Northern hemisphere, we consider $A > 0$ when the normal to the ground (pointing away from the ground) points South, and $A < 0$ otherwise. Of course, A can only take meaningful values from a technical point of view. We shall at least assume $A \in [0, \lambda]$ (°) in order to compare with the horizontal axis tracker and the Polar one.

For values $A < 0$, the value $A_{\min}$ of the solar height $-\alpha_s$ on day 355 at noon is relevant: if $A < A_{min} < 0$, then $T_{B_1} > 12$ and $T_{B_2} < 12$ so that the tracker should rotate suddenly from $-\beta_M^A$ to β_M^A at noon, and it would never work as a true tracker on the days for which those inequalities hold for T_{B1} and T_{B1}. Equivalently, this means that $\cos\theta < 0$ around noon on those days.

As a consequence, we shall restrict ourselves to $A \in [-A_{min}, \lambda]$.

4. Daily solar irradiation incident on a single-axis tracker with tilted axis

The theoretical aim of the motion of a solar tracker is to maximize the daily irradiation reaching its panels, $H_t(n)$ (Wh/m^2):

$$H_t(n) = \int_{T_R(n)}^{T_S(n)} I_t(n,T)dT \tag{27}$$

where $I_t(n,T)$ is the instantaneous solar irradiance (W/m^2), n is the day of the year (day), T is the solar time (h), and $T_R(n)$, $T_S(n)$ are the sunrise and sunset solar times (h). The subindex t is used to denote that the axis of the tracker may be tilted.

The irradiance I_t is divided into three components: beam, diffuse, and ground-reflected. The first one can be calculated from the geometrical relations between horizontal and tilted surfaces [37], for a clear day. Two different models (isotropic and anisotropic), are used for estimating the diffuse component. Previous studies [40–42] have used Liu and Jordan's model [43] with very good results, and this is the model we shall use.

We stress that, assuming isotropy, the Liu-Jordan model [43] aims to collect, in an elementary formula, two facts: (i) that the diffuse solar irradiance reaching a surface is maximum when the surface is parallel to the ground pointing up and minimum when it is parallel to the ground pointing down; (ii) that the ground-reflected irradiance reaching a surface works the opposite way. These two facts are also included in other models, as the: Hay-Davies model [44] and the Perez model [45]. On a different note, Mehleri et al. [46] have compared several isotropic ([43,47–49]) and anisotropic models ([50–56]). Their work shows that the most accurate results were obtained with the Liu-Jordan one [43]. Hence, it is commonly recommended for forecasting the diffuse irradiance reaching a surface at locations throughout the world ([37,57,58]).

In order to take into account the terrain slope A, we must adjust the model. We propose the new formula, which we shall use henceforth in this work:

$$I_t(A,n,T) = I_{bh}(n,T)\cdot R_b + I_{dh}(n,T)\cdot\left(\frac{1+\cos\beta^A}{2}\right) + \left(I_{bh}(n,T)+I_{dh}(n,T)\right)\cdot\rho_g\cdot\left(\frac{1-\cos\beta^A}{2}\right) \tag{28}$$

where $I_{bh}(n,T)$ (W/m^2) is the beam irradiance on a horizontal surface, R_b is called beam radiation tilt factor, $I_{dh}(n,T)$ (W/m^2) is the diffuse irradiance on a horizontal surface, and ρ_g is the dimensionless ground reflectance.

The geometric factor R_b, the ratio of beam radiation on the tilted surface to that on a horizontal surface at any time, can be calculated exactly by the ratio of the cosines of incidence and zenith angles [37]:

$$R_b = \frac{\cos\theta}{\cos\theta_z} \tag{29}$$

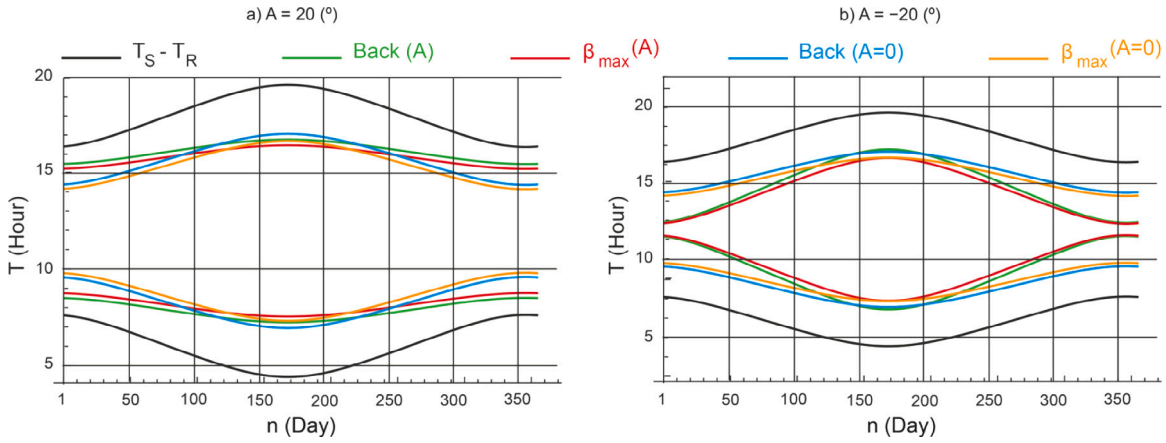

Fig. 5. Influence of A on the operating periods in Gijón.

R_b is a pure geometric parameter, dependent on the horizontal tilt, surface azimuth, declination angle and latitude.

In order to take into account the three operating periods (see Table 2) when computing the irradiation H_t, we divide the operating span $[T_R, T_S]$ into three intervals, being careful to use the right tilt angle β^A and the corresponding cosine of the incidence angle $\cos\theta$:

$$H_t(A,n) = \int_{T_R(n)}^{T_S(n)} I_t(A,n,T)dT \tag{30}$$

4.1. Performance indicator: Energy gain

The concept of energy gain is very useful when evaluating the influence of terrain slope on the performance of single-axis tracker aligned with the North–South axis. Its value EG_A is defined as:

$$EG_A = \frac{H_t^A - H_t^0}{H_t^0} \times 100 \tag{31}$$

where H_t^0 (MWh/m^2) is the total solar irradiation for the installation on flat terrain, and H_t^A (MWh/m^2) is the total solar irradiation for the installation on sloping terrain. In later sections, we shall compute EG_A for N-S aligned single-axis trackers for the values $A = \lambda/4$, $A = \lambda/2$, $A = 3\lambda/4$ and $A = \lambda$.

5. Numerical simulations

In this section we present the numerical simulations corresponding to the location of the experimental setup: Latitude $43°31'22''N$, Longitude $05°43'07''W$, elevation 28 (m) above sea level (Electrical Engineering Department of the University of Oviedo (Gijón, Spain)).

We simulate the effect of the slope (always N-S) of the terrain on various parameters, as the cos θ and the annual energy using Mathematica to compute the three components of the total solar irradiance. We have made two simulations, corresponding to:

(i) The classic Hottel and Liu and Jordan's clear-sky models.

(ii) A cloudy-sky model. In order to take into account the meteorological conditions of the location, we use the method proposed in [59], whose inputs are the monthly-averaged beam and diffuse solar irradiation. We have used satellite-derived $PVGIS$ data [60].

5.1. Influence of the terrain slope on $\cos\theta$

Usually, the orientation of solar trackers is chosen considering only the beam irradiance, so that the energy generated by the PV system is mainly influenced by $\cos\theta$. This motivates Fig. 6, which is based on Eq. (16). It contains six different plots of the values of $\cos\theta$ in Gijón (Spain) for each day n of the year, at all hours T, (from sunrise to sunset). Each plot corresponds to a value of the longitudinal tilt angle A, distributed between 0 (°) and 1.25λ (°), where $\lambda = 43$ (°) is the latitude.

Notice how, as A increases with $A \le \lambda$, the value of $\cos\theta$, increase too, and get closer to 1. The distribution is, however, far from homogeneous in n and T. For $A = \lambda$, we get the well-known equality $\cos\theta = \cos\delta$, characteristic of the polar trackers. If $A > \lambda$ increases, the value of $\cos\theta$ decreases.

In general, a positive slope A improves the values of $\cos\theta$ as long as $A \in [0, \lambda]$, but in a highly non-linear way. Notice how the polar tracker is optimal around noon for most of spring, autumn, and winter, but near the summer solstice ($n = 174$), it is outperformed by trackers with less tilt angle. This influences, as we show later on, the total energy production of each tracker.

5.2. Influence of the terrain slope on annual energy

The annual absorbed energy is computed, from (27), depending on the terrain slope A, as:

$$H_a(A) = \sum_{n=1}^{365} H_t(n,\beta,\gamma) \tag{32}$$

We performed two simulations:

(i) A clear-sky model which comprises Hottel's [61] for beam irradiance, and Liu-Jordan's [62] for beam and diffuse. The values of H_a depending on A are plotted in Fig. 7. Notice how $A = 0$ (°) gives the minimum value of H_a, and this increases with A up to the maximum $H_a = 2.65199$ (MWh/m^2), which in this case is attained for $A = 37.5$ (°). Remarkably, this maximum does not correspond to $A = 43.52$ (°) (the latitude of the location, also the tilt corresponding to the polar tracker). We hypothesize that this is mainly due to the influence of the diffuse and reflected irradiance, as well as the already mentioned non-linear variation of $\cos\theta$ with A. In any case, for the clear-sky model the horizontal tracker is the worst option.

(ii) A Cloudy-sky model following [59], which takes into account the particular weather conditions of the location (see Fig. 8). The values of H_a depending on A behave differently from the previous case. First (and obviously), there is a remarkable decrease in absorbed energy, as Gijón is a rather cloudy place. Secondly, the maximum value $H_a = 1.63111$ (MWh/m^2) occurs now for $A = 40.00$ (°), which happens to be nearer to the tilt of the polar tracker but without an obvious explanation.

Table 3 contains the annual solar irradiation and the energy gain with respect to the horizontal tracker, for Gijón in the cloudy-sky model, for $A = 0$, $\lambda/2$, λ, which the values we have tested experimentally.

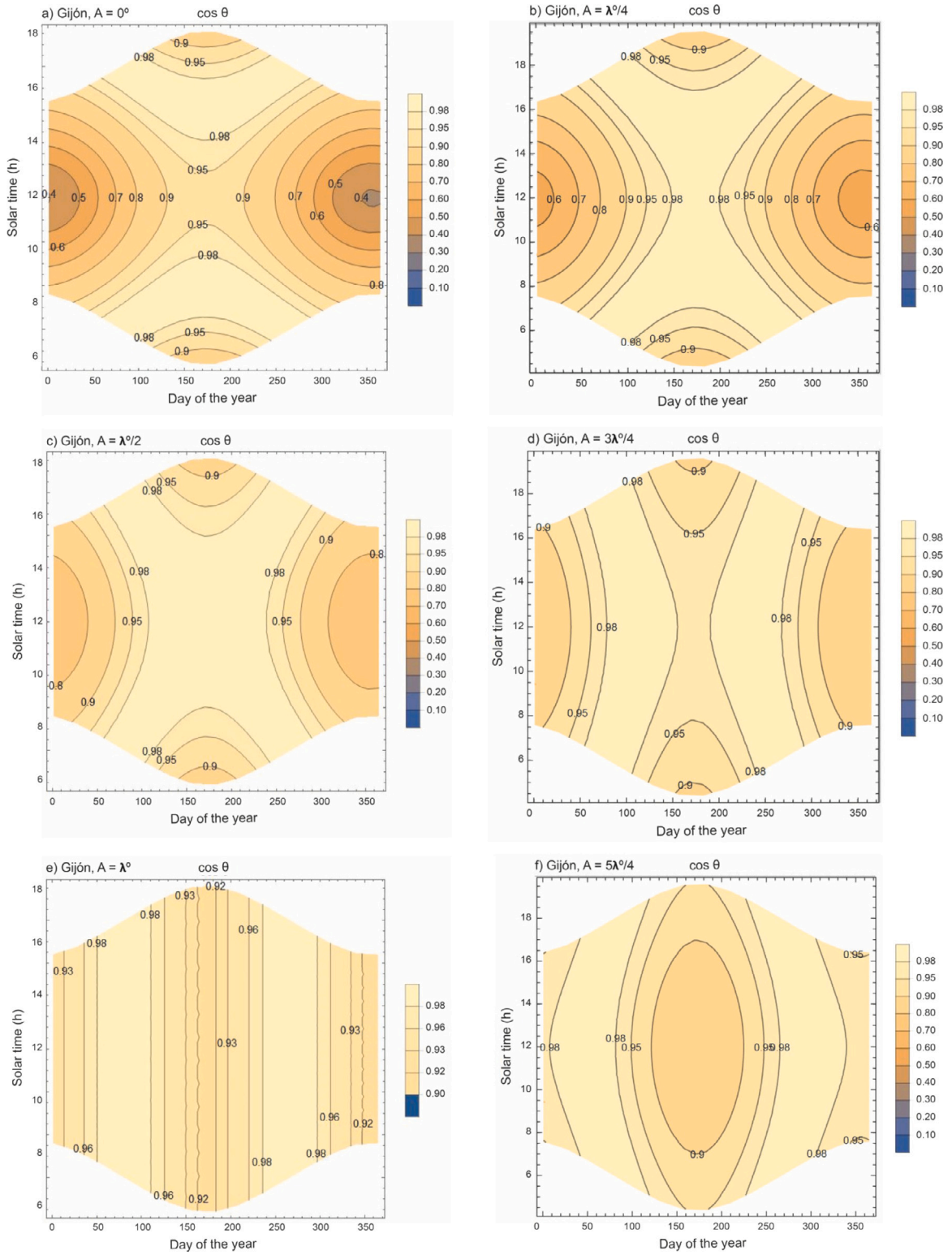

Fig. 6. Values of $\cos\theta$ or the location in Gijón.

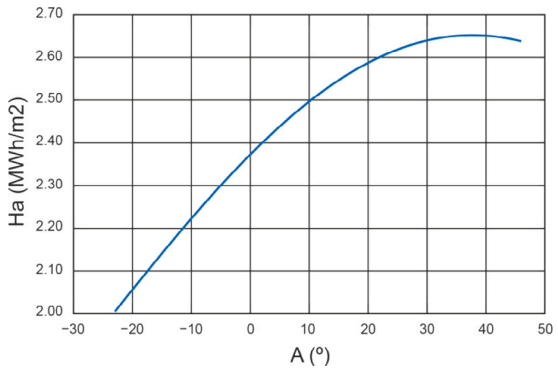

Fig. 7. H_a(A)for clear sky-model.

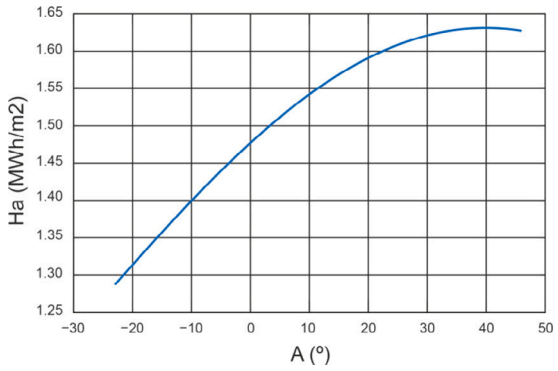

Fig. 8. H_a(A) for cloudiness sky-model.

Table 3
Annual solar irradiation and energy gain.

Parameter	Terrain slope (°)		
	0	$\lambda/2$	λ
Annual solar irradiation (MWh/m^2)	1.4772	1.5985	1.6298
Energy gain (%)	–	8.21	10.33

Finally, Fig. 9 shows the monthly energy gain for $A = \lambda/2$ (°) and $A = \lambda$ (°), and their different behavior in summer and winter. Due to the solar declination, the polar tracker even incurs a loss around the summer solstice, when the declination is maximum. On the other hand, when the solar declination is minimum, the gain es greatest.

6. Experimental setup

Our tests have used a prototype of a N-S aligned single-axis tracker with different simulated terrain slopes. We have gathered 12 full months' of total solar irradiance at the location of the Department of Electrical Engineering of the University of Oviedo, in Gijón, Spain (Latitude $43^o31'22''$, Longitude $05^o43'07''W$, elevation 28 (m) above sea level). It comprises a structural system and the tracking system.

The structural system has three columns and purlins, and an axis (see Fig. 10). It is covered with a surface treatment of Hot-Dip Galvanizing, and holds 8 PV modules mounted on the purlins by clamps.

The tracking system consists of a transmission system (three spherical bearings), DC motor and drivers, and an electronic control module. It uses a single engine, which rotates the PV modules from East to West on a horizontal axis, following the daily motion of the Sun. Its rotation range is ±60 (°) with respect to the horizontal.

6.1. Measuring equipment

We installed three pyranometers on the tracker in order to measure the total irradiance reaching a plane tilted with respect to the N-S axis. Thus, they are N-S aligned and facing South.

Pyranometer 1 is mounted on the edge of the PV module and is used to measure the beam irradiance on a horizontal plane, that is: $A = 0$ (°) Pyranometer 2 is mounted with a longitudinal tilt angle $A = \lambda$ (°), and Pyranometer 3 is mounted with a longitudinal tilt angle $A = \lambda/2$ (^{o}). Fig. 11 contains the schematics. The sensors are Kipp & Zonen RT1, with specifications summarized in Table 4.

Two additional pyranometers are required to assess the global solar on the horizontal plane (Pyranometer 4) and the diffuse irradiance on the horizontal plane (Pyranometer 5). The former was recorded with a Kipp & Zonen CMP11 Secondary Standard pyranometer. The latter with a Kipp & Zonen CMP11 Secondary Standard pyranometer and a shadow ring. Their specifications are summarized in Table 4. The pyranometers are periodically calibrated to ensure the traceability of the measurements. Solar irradiance measurements were made with a 1 (s) time step and then integrated to bring them to a 1 (min) time step.

The measuring devices CMP11 and TR1, are thermopile sensors, so that they provide indirect data with several sources of uncertainty (see [63]). Their specifications indicate that the uncertainty levels for daily totals are $< 2\%$, which we is acceptable [64].

6.2. Experimental procedure

At the laboratory of the research group "Energy Conversion for Sustainable Development" [65] of the Department of Electrical Engineering of the University of Oviedo (in Gijón, Spain), a single tracker system was installed and has been used as a prototype for verifying our results. As single trackers do not have any shading issues, it does not do any backtracking, and it has just two modes of operation: static, and normal tracking, covering three time intervals on each single day.

The lack of backtracking in our prototype should not affect the relevance of the experimental results: as we said above, the inclusion of the slope A causes two opposite effects: during a part of the year, the normal tracking period gets longer, whereas on the complementary days, the operating period gets shorter due to the apparition of intervals in which the cosine of the incidence angle is negative (the Sun is "behind" the tracker"). These two effects are practically equivalent and cancel each other out, so that in the end, our values of EG_A are realistic.

We remark that the climate of Gijón, is temperate oceanic, with mild, rainy winters and cool, relatively rainy summers, and high occurrence of clouds. The degree of cloudiness has been quantified as the "cloudiness index" [66,67], which is the ratio between the diffuse irradiance and the global irradiance (so that it is less than 1), both on the horizontal plane. It is usually divided into three intervals ranging from 0 (clear sky) to 1 (overcast) [67]: clear $(0.00, 0.33)$, partial $(0.33, 0.8)$ and cloudy $[0.8, 1)$. To ensure the correctness and reliability of our results, the experiments were performed on all types of days, for 9 (h) each day, from 9 : 00 to 18 : 00 local time.

The longitudinal tilt angles we have studied are $A = 0$ (°), $A = \lambda/2$ (°) and $A = \lambda$ (°). Recall that $\lambda = 43.52$ (°) for our experiments.

7. Experimental results and discussion

We now present our experimental results. Data collection corresponds to the 12 months of 2022. All the energy gain data is relative to the horizontal tracker (that is, $A = 0$ (°)).

Fig. 12 shows the energy gain for each month of the year, for $A = \lambda/2$ (°) and $A = \lambda$ (°). Notice the remarkable similarity of the trend of the theoretical and experimental results, and the good fit of the simulation for both values of A. This, in our view, is a clear validation of our theoretical model and the numerical simulations.

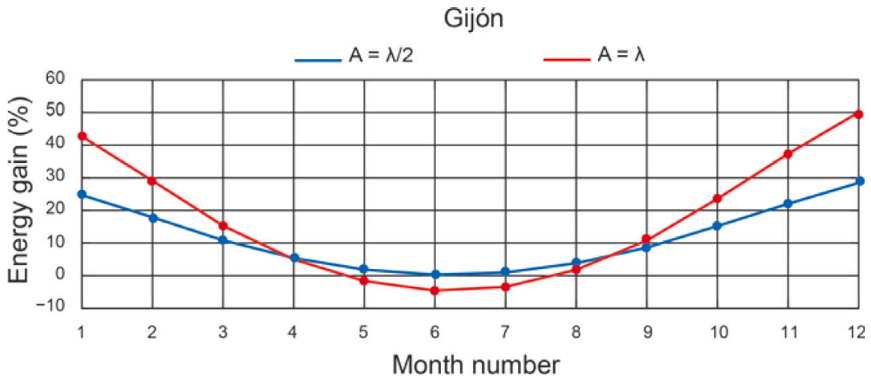

Fig. 9. Comparison of monthly energy gain.

Table 4
Characteristics of the pyranometers used in the tests.

n°	Type Kipp & Zonen	Specifications	Azimuth angle	Longitudinal tilt angle
1	TR1	Range: 0–2000 (W/m^2) Precision/resolution: 1 (W/m^2)	0 (S facing)	0
2	TR1	Range: 0–2000 (W/m^2) Precision/resolution: 1 (W/m^2)	0 (S facing)	$\lambda/2$
3	TR1	Range: 0–2000 (W/m^2) Precision/resolution: 1 (W/m^2)	0 (S facing)	λ
4	CMP11	Range: 0–4000 (W/m^2)tabbr Expected daily accuracy: < 2%	–	–
5	CMP11	Range: 0–4000 (W/m^2) Expected daily accuracy: < 2%	–	–

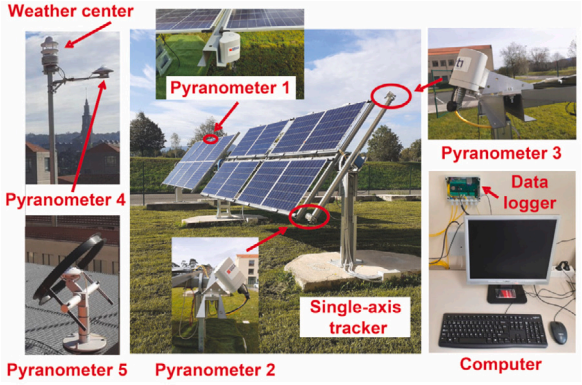

Fig. 10. Experimental setup.

We attribute the differences between the experimental and the theoretical data to several factors:

(i) The discretization used in the motion of the tracker, which is necessarily different to the one used to integrate the irradiance in the simulation.
(ii) The motion of the tracker is the same for pyranometers 1, 2 and 3. Therefore, the tracking of the Sun is not exactly the one it should be, and the results are somewhat worse than the real ones.
(iii) The solar irradiance model [59] uses, necessarily, past data (averaged for a span of 10 years) to predict what the experiment does measure.

To provide a deeper view of the curves in Fig. 12, we have analyzed three specific years under each of the typical daily meteorological conditions: 3 sunny days, 1 partly cloudy day, and 3 cloudy days. We limit ourselves to 7 days for the sake of brevity, but data is available for the 365 days recorded. We have chosen days with the most stable solar irradiance have been chosen. The results are plotted in Fig. 13, Figs. 14 and 15. All the experimental data correspond to the year 2022.

In Fig. 13 the total solar irradiance on three sunny days, at each time of the day, is plotted, for values of $A = 0$, $\lambda/2$ and λ (°). Fig. 13.a corresponds to February 2, which had a cloudiness index of 0.13. The system with $A = \lambda$ (°) receives the most solar irradiance at practically all times, and the one with $A = 0$ (°) receives the least. These data match those shown in Fig. 9 for month 2.

Fig. 13.b corresponds to July 1, which had a cloudiness index of 0.10. In this case, the system with $A = \lambda/2$ (°) is the most performance, overall, whereas noticeably, the one with $A = \lambda$ is the worst. These result match those given in Fig. 9 for month 7.

Fig. 13.c corresponds to September 9, 2022, with a cloudiness index of 0.15. In this case, the systems with $A = \lambda$ (°) and $A = \lambda/2$ (°) are practically indistinguishable, whereas the one with $A = 0$ (^{o}) is clearly worse. These results match those given in Fig. 9 for month 9.

We can thus assert that for sunny days, our experimental results validate our theoretical and numerical models.

Fig. 14 shows the total solar irradiance on three specific cloudy days, with terrain slopes $A = 0$ (°), $A = \lambda/2$ (°), and $A = \lambda$ (°).

Specifically, we chose July 22 (Fig. 14.a), which had a cloudiness index of 0.88, August 30 (Fig. 14.b), with cloudiness index of 0.92, and December 9 (Fig. 14.c), with 0.98. The profiles of the solar irradiance received by the system are very similar. We claim this is due to the predominance of the diffuse component of the irradiance, and the low beam component, so that the tracking has no influence on the total irradiation received. It is well-known that on these days, the optimal position of the tracker is the one maximizing the diffuse component.

As regards partly cloudy days, we have just chosen August 18, with a cloudiness index of 0.38 to illustrate our results, shown in Fig. 15. The profiles of the three curves are similar during the cloudy period and the differ in the way Fig. 9 indicates for month 8, during the rest of the day.

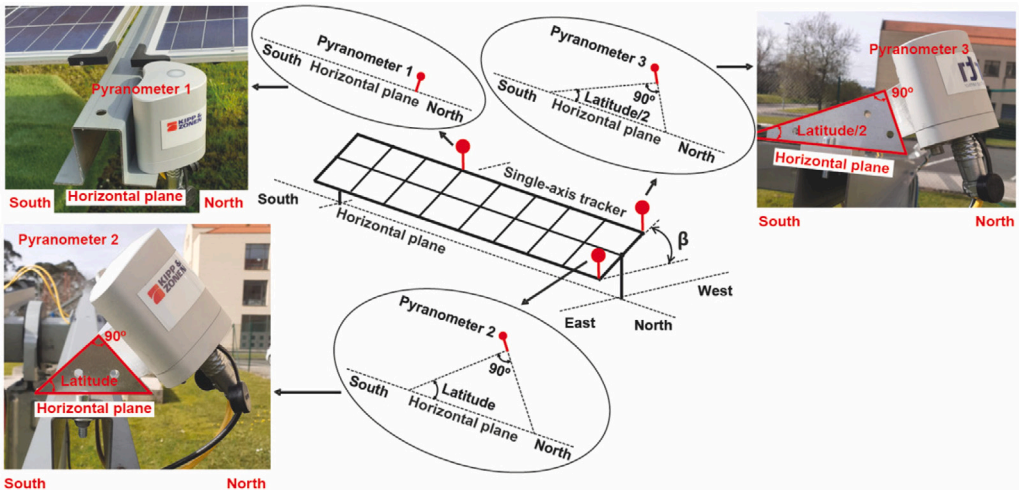

Fig. 11. Schematic diagram.

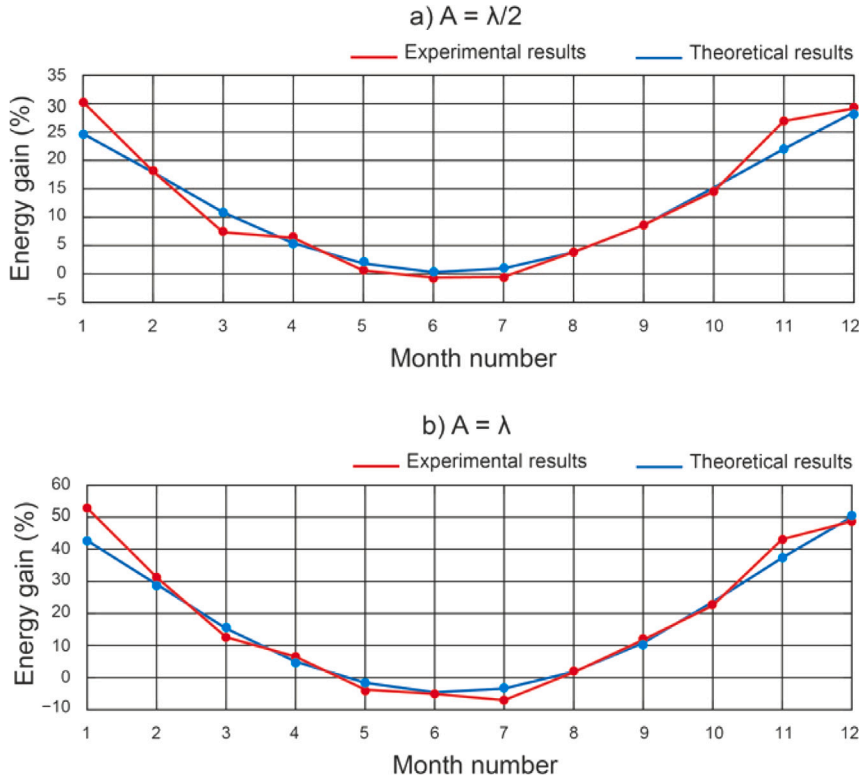

Fig. 12. Comparison of monthly energy gain.

8. Simulated estimations for locations around the world

In this section, we simulate our method for different locations around the northern hemisphere. We have developed Mathematica code to carry out the computations for each component of the solar irradiance. The beam and diffuse components have been calculated with the method proposed in [59], whose inputs are the monthly-averaged beam and diffuse solar irradiation. These data have been obtained from satellite-derived $PVGIS$ data [60] for the each location. Each site belongs to a different climatic area and its latitude is different enough to allow for meaningful comparison. We study 10 locations covering from 6 (°) to 60 (°) North latitude, with a step of 6 (°), approximately. Table 5 summarizes their geographic characteristics.

Using Eq. (27), the annual energy is calculated as a function of the variation of the terrain slope, while also considering the effects of the different weather conditions. Table 5 contains the values of annual solar irradiation for each value of λ. Notice how $A = 0$ (°) corresponds, consistently, to the least value. Generally (but not always), increasing the terrain slope corresponds to an increase in the annual energy up to $A = 3\lambda/4$ (°). Between $A = 3\lambda/4$ (°) and $A = \lambda$ (°), the total energy increases up to $\lambda \simeq 30$ (°) (Cairo), and then the value decreases consistently (see Table 6).

Fig. 16 shows of annual energy gain in the locations under study.

Fig. 16 suggests the following inferences (energy gains are with respect to the baseline $A = 0$ (°)).

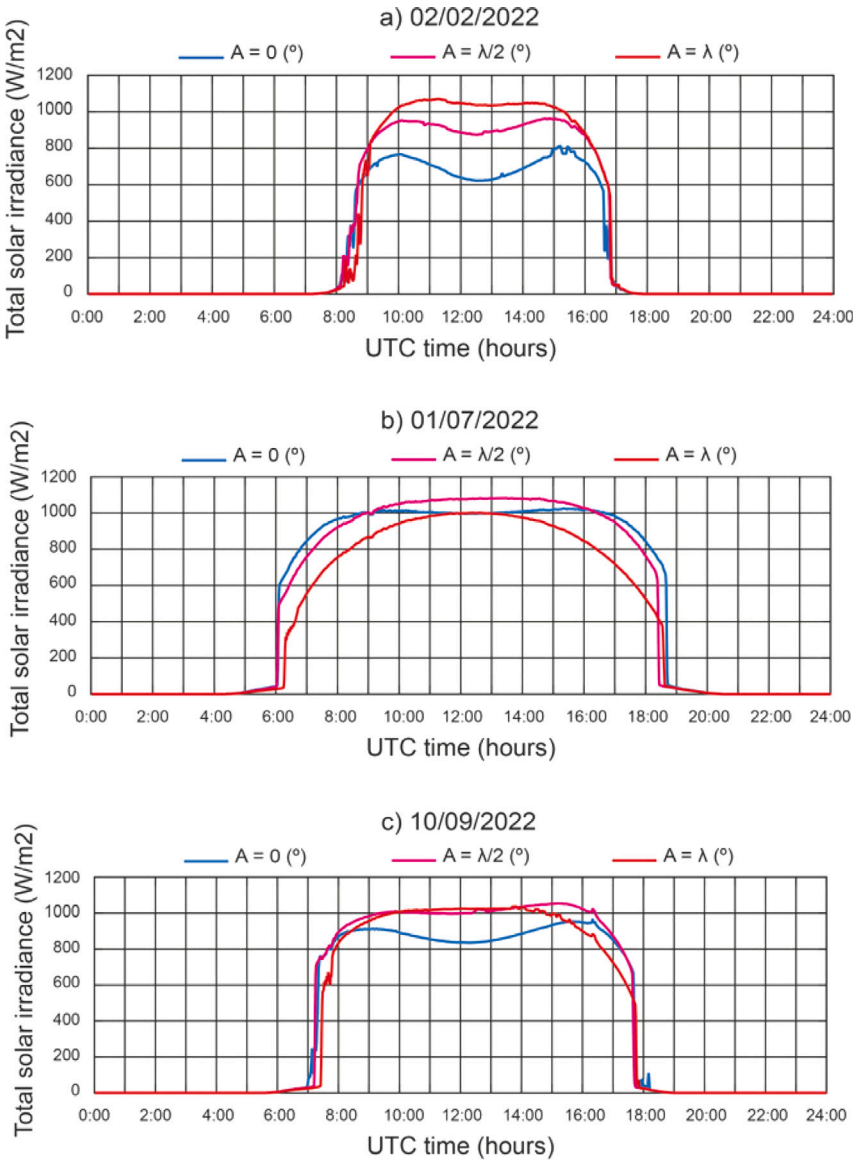

Fig. 13. Comparison of total solar irradiance on sunny days.

Table 5
Locations under study.

	Locations	Latitude	Longitude	Altitude
1	Medellin (Colombia)	06°14′38″ N	75°34′04″ W	1469 (m)
2	Bangkok (Thailand)	13°45′14″ N	100°29′34″ E	9 (m)
3	Morelia (Mexico)	19°42′10″ N	101°11′24″ W	1921 (m)
4	Karachi (Pakistan)	24°52′01″ N	67°01′51″ E	14 (m)
5	Cairo (Egypt)	30°29′24″ N	31°14′38″ W	41 (m)
6	Almeria (Spain)	36°50′07″ N	02°24′08″ W	22 (m)
7	Toronto (Canada)	43°39′14″ N	79°23′13″ W	106 (m)
8	Wien (Austria)	48°15′00″ N	16°21′00″ E	203 (m)
9	Hamburg (Germany)	53°33′00″ N	10°00′03″ E	19 (m)
10	Helsinki (Finland)	60°10′10″ N	24°56′07″ E	23 (m)

Table 6
Annual solar irradiation (MWh/m^2).

Location	Terrain slope (°)				
	0	$\lambda/4$	$\lambda/2$	$3\lambda/4$	λ
Medellin (Colombia)	2.1371	2.1390	2.1403	2.1411	2.1412
Bangkok (Thailand)	2.1543	2.1673	2.1773	2.1841	2.1878
Morelia (Mexico)	2.6730	2.7069	2.7324	2.7491	2.7568
Karachi (Pakistan)	2.5858	2.6381	2.6771	2.7023	2.7131
Cairo (Egypt)	2.7169	2.7847	2.8309	2.8542	2.8540
Almeria (Spain)	2.4907	2.5872	2.6537	2.6873	2.6866
Toronto (Canada)	1.6220	1.6939	1.7430	1.7664	1.7627
Wien (Austria)	1.4977	1.5752	1.6279	1.6520	1.6457
Hamburg (Germany)	1.3021	1.3860	1.4432	1.4684	1.4595
Helsinki (Finland)	1.1919	1.2770	1.3328	1.3529	1.3349

(i) An increase in terrain slope, up to $A = 3\lambda/4$ (°) increases the energy generated, an effect which is most pronounced as latitude increases. For $\lambda \leq 30$ (°), this is also true for $A = \lambda$ (°).
(ii) Energy gains range from 0.08% (low latitude) to 13.50% (high latitude).
(iii) For small λ (Medellin) the maximum energy gain is only 0.19%.
(iv) Up to $\lambda = 30$ (°), corresponding to Cairo, energy gains are consistently larger for larger A.
(v) For latitudes above Cairo, the maximum energy gain is obtained for $A = 3\lambda/4$ (°).

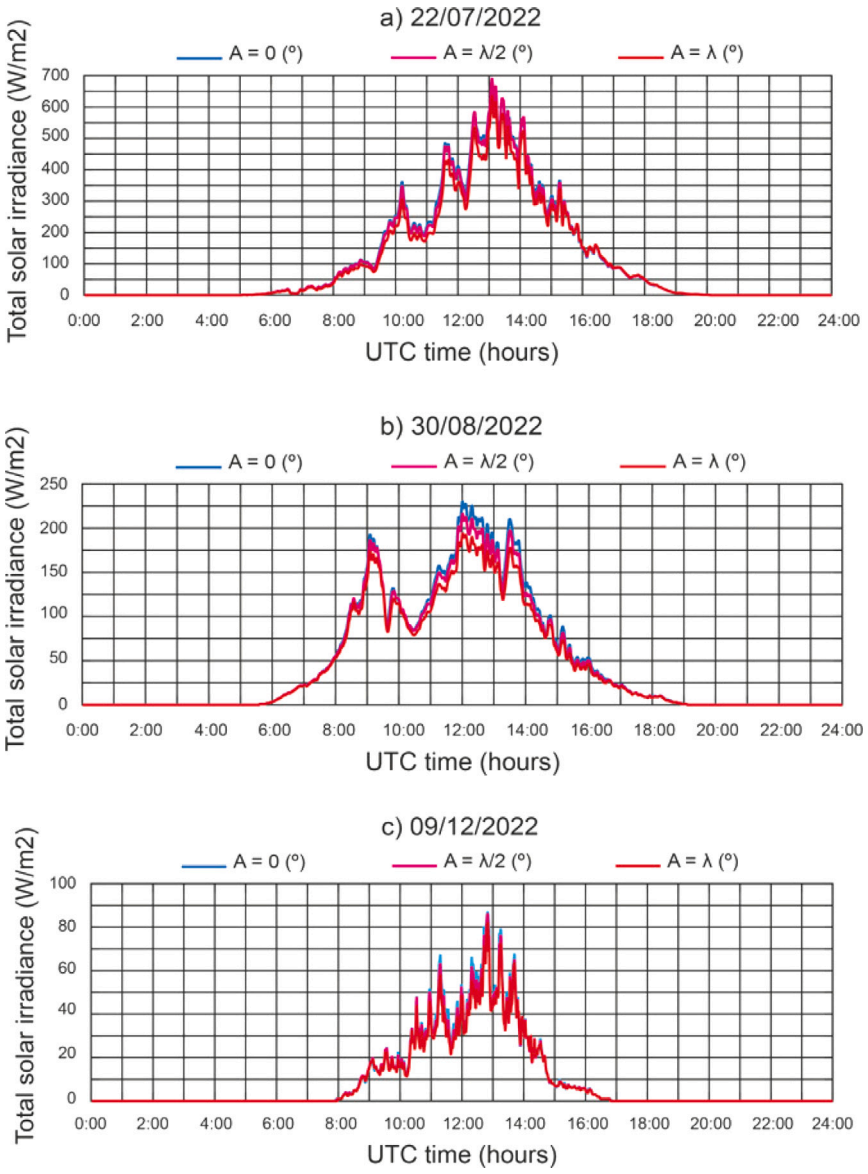

Fig. 14. Comparison of total solar irradiance on cloudy days.

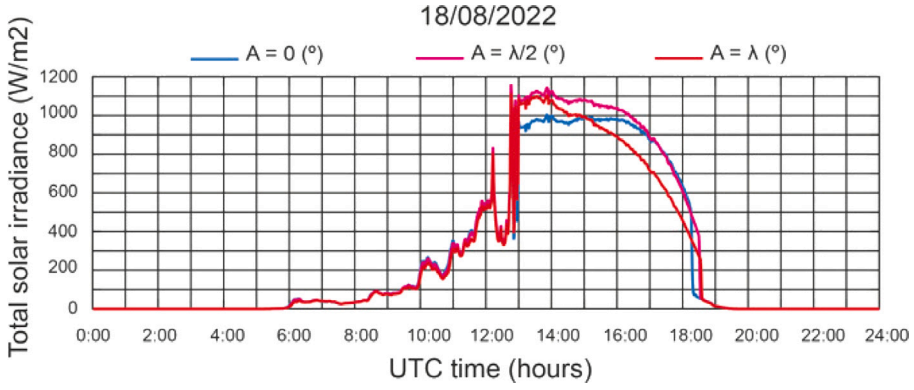

Fig. 15. Comparison of total solar irradiance on a partly cloudy day.

In our study, the impact of the slope for low-latitude locations is small, as it should, because we take A between 0 and the latitude λ. Even more, at these latitudes, the Sun altitude is greater, which reduces the effect of the slope (due to the maximum of the cosine function at 0). On the contrary, at higher latitudes, the lower Sun altitude gets compensated remarkably more and more (A between 0 and λ) due to the non-linear positive effect of the slope of the terrain, and the derivative of the cosine function being nonzero away from 0.

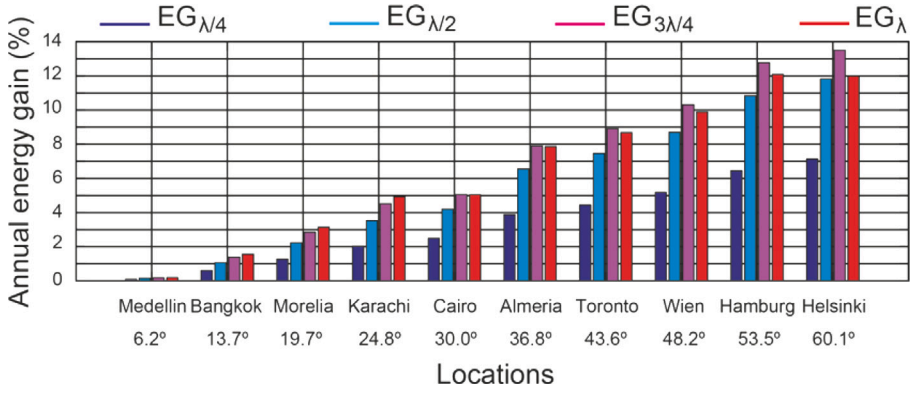

Fig. 16. Annual energy gain at each location.

Fig. 17 shows the data corresponding to the monthly energy gain with respect to the horizontal tracker at each location.

Notice how, at higher latitudes, the energy gain in the months with negative solar declination is much higher. However, losses are at most 10% in the months with positive declination. For lower latitudes, the differences are much less. In Medellin, for instance, the maximum energy gain is less than 3%, and the minimum is −2.5%. This shows how the slope of the terrain is much more relevant at higher latitudes, as is logical.

9. Conclusions and future perspectives

In this work the formulas governing the motion of a single-axis solar tracker on sloped terrains are verified. A field experiment design and setup are described to evaluate the influence of the terrain slope on the irradiance received by such a system, by measuring the hourly solar irradiance received by the tracker on horizontal terrain, and on slopes equal to the latitude and mid-latitude. The first one is taken as baseline. Data has been produced daily during the whole year 2022. Experimental and numerical results have been compared, by means of the energy gain, so as to estimate the influence of terrain slope on the performance. Finally, simulations at 10 locations in the northern hemisphere are carried out and analyzed. The main conclusions are:

(i) Monthly energy gain varies throughout the year, depending mainly on the solar declination. Consistently, there is an inverse correlation between solar declination and energy gain, both in the experimental data, and for all the simulated slopes and locations.
(ii) The previous assertion holds also for sunny days.
(iii) In general, increasing the slope (up to the latitude) increases the energy gain, and the effect is stronger at highest latitudes. There is, however, a maximum for the slope equal to 3/4 the latitude, after which the gain decreases at latitudes greater than 30 (°).
(iv) The percentage of the energy gains due to the slope, with respect to the horizontal tracker, ranges from 0.08% (low latitude) to 13.50% (high latitude). In Medellin (lowest latitude), the energy gain is at most 0.19%, whereas in Helsinki (highest latitude), the energy gain reaches 13.50%.

Given that wind farms are often located in regions that are difficult to access, with steep slopes, we believe that this work can be continued with a joint study of wind farms and solar plants in mountainous regions. The significant cost of construction of the road network and the electric transmission lines would in this case be shared between the two power plants, favoring their economic profitability.

CRediT authorship contribution statement

A. Barbón: Conceptualization, Methodology. **P. Fortuny Ayuso:** Methodology, Software. **L. Bayón:** Conceptualization, Methodology. **C.A. Silva:** Methodology, Software, Writing – original draft.

Declaration of competing interest

The authors declare that they have no known competing financial interests or personal relationships that could have appeared to influence the work reported in this paper.

Data availability

No data was used for the research described in the article.

Acknowledgments

We wish to thank Gonvarri Solar Steel [23] for their contributions to this study.

Appendix. Computation of the tilt angle

The tilt angle β, which is the angle between the axis of the collector surface and the normal to the horizontal plane is given, in the local system (S′), by:

$$\cos\beta = \overline{n}_p \cdot \overline{k'} \tag{33}$$

As $\overline{n}_p$ has the following expression in the local system:

$$\overline{n}_p = (\sin\beta^A, 0, \cos\beta^A)\cdot(\overline{i''}, \overline{j''}, \overline{k''}) \tag{34}$$

$$= (\sin\beta^A, 0, \cos\beta^A)\cdot\begin{pmatrix}1 & 0 & 0\\ 0 & \cos A & -\sin A\\ 0 & \sin A & \cos A\end{pmatrix}\cdot\begin{pmatrix}\overline{i'}\\ \overline{j'}\\ \overline{k'}\end{pmatrix}$$

$$\overline{n}_p = (\sin\beta^A, \cos\beta^A\sin A, \cos\beta^A\cos A).(\overline{i'}, \overline{j'}, \overline{k'})$$

We obtain:

$$\cos\beta = \overline{n}_p \cdot \overline{k'} = \cos\beta^A\cos A \tag{35a}$$

And using the equalities:

$$\cos\beta^A = \frac{C_2}{\sqrt{C_1^2 + C_2^2}};\quad \cos\theta_i = \sqrt{C_1^2 + C_2^2} \tag{36}$$

We get the following formula for β:

$$\beta = \text{sign}(\omega)\cdot\arccos\left[\cos A\frac{\cos\omega\cos\delta\cos(\lambda - A) + \sin\delta\sin(\lambda - A)}{\cos\theta_i}\right] \tag{37}$$

Sign convention: $\beta < 0$ before noon and $\beta > 0$ after.

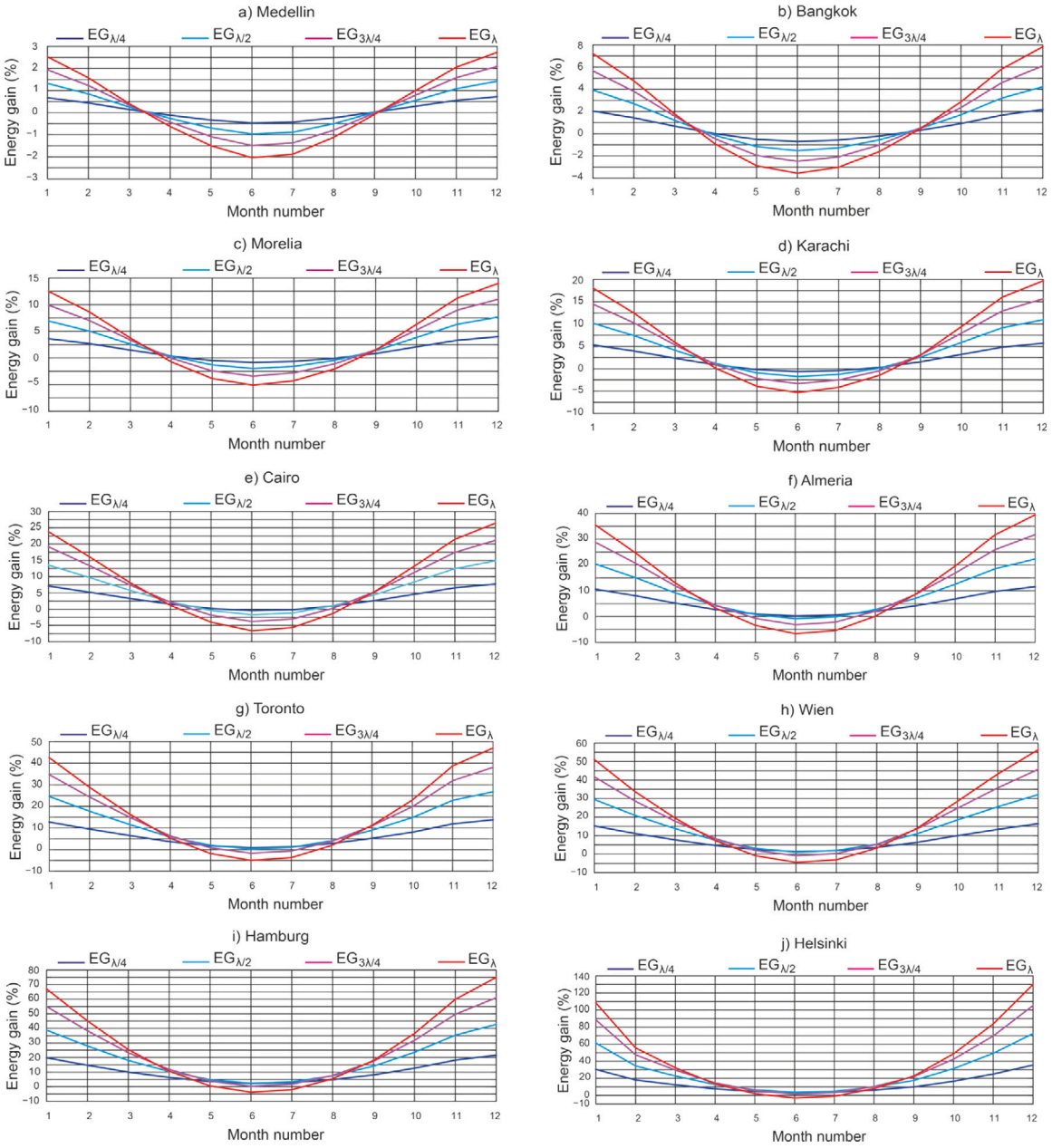

Fig. 17. Monthly energy gain for the locations under study.

Eq. (37) includes the N-S Horizontal ($A = 0$) and Polar ($A = \lambda$) cases in [37]:

$$(i)\ A = 0 \Rightarrow\ \beta = \arctan[\tan\theta_z \sin\gamma_s]$$
$$(ii)\ A = \lambda \Rightarrow\ \beta = \arccos[\cos\lambda\cos\omega]$$

where θ_z is the zenith angle of the Sun, and γ_S the azimuth of the Sun.

2. *Computation of the azimuth angle*

The azimuth γ of the collector surface is the angle between the projection $\overline{v}$ of $\overline{n}_P$ on the horizontal plane and Oy' in the local system (S'). The latter is given by:

$$\overline{n}_p = (\sin\beta^A, \cos\beta^A \sin A, \cos\beta^A \cos A).(\overline{i'}, \overline{j'}, \overline{k'}) \tag{38}$$

So that:

$$\overline{v} = (\sin\beta^A, \cos\beta^A \sin A, 0).(\overline{i'}, \overline{j'}, \overline{k'}) \tag{39}$$

As a consequence:

$$\cos\gamma = \frac{\overline{v}\cdot\overline{j'}}{|\overline{v}|} = \frac{\cos\beta^A \sin A}{\sqrt{\sin^2\beta^A + \cos^2\beta^A \sin^2 A}} = \frac{\sin A}{\sqrt{\tan^2\beta^A + \sin^2 A}} \tag{40}$$

Which gives:

$$\gamma = \text{sign}(\omega)\cdot\arccos\left[\frac{\sin A\ (\cos\omega\cos\delta\cos(\lambda - A) + \sin\delta\sin(\lambda - A))}{\cos\delta\sqrt{\sin^2\omega + \sin^2 A(\cos\omega\cos(\lambda - A) + \tan\delta\sin(\lambda - A))^2}}\right] \tag{41}$$

Sign convention: $\gamma < 0$ before noon and $\gamma > 0$ after.

Again, the formula above includes the N-S Horizontal ($A = 0$) and Polar ($A = \lambda$) cases [37]:

$$(i)\ A = 0 \Rightarrow\ \gamma = \begin{cases} 90° & \text{si} \quad \gamma_s > 0° \\ -90° & \text{si} \quad \gamma_s \le 0° \end{cases}$$

$$(ii)\ A = \lambda \Rightarrow\ \gamma = \arccos \frac{1}{\sqrt{1 + \frac{\tan^2 \omega}{\sin^2 \lambda}}}$$

References

[1] bp. Statistical review of world energy. 2021, 70th edition. Available from: https://www.bp.com/content/dam/bp/business-sites/en/global/corporate/pdfs/energy-economics/statistical-review/bp-stats-review-2021-full-report.pdf. [Accessed on 23 March 2023].

[2] bp. Integrated energy company strategy update: Growing investment, growing value, growing distributions. 2023, Available from: https://www.bp.com/en/global/corporate/news-and-insights/press-releases/4q-2022-update-on-strategic-progress.html. [Accessed on 23 March 2023].

[3] Kapos K, Rhind DJ, Edwards M, Price MF, Ravilious C. Developing a map of the world's mountain forests. In: Forests in sustainable mountain development: A state-of knowledge report for 2000. M.F. Price and N. Butt. Wallingford: CAB International; 2000, p. 4–9.

[4] Xu L, Long E, Wei J, Cheng Z, Zheng H. A new approach to determine the optimum tilt angle and orientation of solar collectors in mountainous areas with high altitude. Energy 2021;237:121507.

[5] Chitturi SRP, Sharma E, Elmenreich W. Efficiency of photovoltaic systems in mountainous areas. In: 2018 IEEE international energy conference. p. 1–6.

[6] Aglietti G, Markvart T, Tatnall A. Solar power generation using high altitude platforms feasibility and viability. Prog Photovolt, Res Appl 2008;16:349–59.

[7] Nguyen DB, Nong D, Simshauser P, Nguyen-Huy T. General equilibrium impact evaluation of food top-up induced by households' renewable power self-supply in 141 regions. Appl Energy 2022;306:118126.

[8] Turner R, Newton CM, Dennis DF. Economic relationships between parcel characteristics and price in the market for Vermont forestland. Forest Sci 1991;37:1150–62.

[9] Chen YK, Jon Kirkerud JG, Folsland Bolkesjø T. Balancing GHG mitigation and land-use conflicts: Alternative northern European energy system scenarios. Appl Energy 2022;310:11855.

[10] Lubowski RN, Bucholtz S, Claassen R, Roberts MJ, Cooper JC, Gueorguieva A, et al. Environmental effects of agricultural land-use change: The role of economics and policy. Economic research report Number 25, 2006.

[11] Hemmati A, Tabatabaeefar A, Rajabipour A. Comparison of energy flow and economic performance between flat land and sloping land olive orchards. Energy 2013;61:472–8.

[12] Nabiollahi K, Golmohamadi F, Taghizadeh-Mehrjardi R, Kerry R, Davari M. Assessing the effects of slope gradient and land use change on soil quality degradation through digital mapping of soil quality indices and soil loss rate. Geoderma 2018;318:16–28.

[13] Deng C, Zhang G, Liu Y, Nie X, Li Z, Liu J, et al. Advantages and disadvantages of terracing: A comprehensive review. Int Soil Water Conserv Res 2021;9(3):344–59.

[14] Bianca Tilliger B, Rodríguez-Labajos B, Bustamante JV, Settele J. Disentangling values in the interrelations between cultural ecosystem services and landscape conservation—A case study of the ifugao rice terraces in the Philippines. Land 2015;4(3):888–913.

[15] Duffy M. Economies of size in production agriculture. J Hunger Environ Nutr 2009;4(3–4):375–92.

[16] Geopard. Available from: https://geopard.tech/blog/topography-and-nutrition-content-in-soil-and-yield/. [Accessed on: 15 May 2023].

[17] E. Nyathira Kihiu, Amuakwa-Mensah F. Agricultural market access and dietary diversity in Kenya: Gender considerations towards improved household nutritional outcomes. Food Policy 2021;100:102004.

[18] Ali S, Taweekun J, Techato K, Waewsak J, Gyawali S. GIS based site suitability assessment for wind and solar farms in Songkhla, Thailand. Renew Energy 2019;132:1360–72.

[19] EU Directive 92/43/EEC of 21 1992 On the conservation of natural habitats and of wild fauna and flora.

[20] Barbón A, Ayuso PFortuny, Bayón L, Silva CA. A comparative study between racking systems for photovoltaic power systems. Renew Energy 2021;180:424–37.

[21] Martín-Martínez S, Cañas-Carretón M, Honrubia-Escribano A, Gómez-Lázaro E. Performance evaluation of large solar photovoltaic power plants in Spain. Energy Convers Manage 2019;183:515–28.

[22] Bahrami A, Onyeka Okoye C. The performance and ranking pattern of PV systems incorporated with solar trackers in the northern hemisphere. Renew Sustain Energy Rev 2018;97:138–51.

[23] Gonvarri solar steel. 2023, Available from: https://www.gsolarsteel.com/. [Accessed on 23 March 2023].

[24] Mackenzie Wood. Global solar PV tracker landscape 2020. Wood Mackenzie company 2020. 2023, Available from: https://www.woodmac.com/reports/power-markets-the-global-solar-pv-tracker-landscape-2020-437508/. [Accessed on 13 May 2023].

[25] Mousazadeh H, Keyhani A, Javadi A, Mobli H, Abrinia K, Sharifi A. A review of principle and sun-tracking methods for maximizing solar systems output. Renew Sustain Energy Rev 2009;13(8):1800–18.

[26] Lv H, Zheng Y, Wang J, Chen B, Sheng F, Cheng C, et al. Tracking control and output power optimization of a concentrator photovoltaic system with polar axis. Optik 2016;127:3840–3.

[27] Shingleton J. One-axis trackers–Improved reliability, durability, performance, and cost reduction. Final subcontract technical status report, 2 May 2006-31 August 2007 (No. NREL/SR-520-42769), Golden, CO (United States): National Renewable Energy Lab. (NREL); 2008.

[28] Li Z, Liu X, Tang R. Optical performance of inclined south-north single-axis tracked solar panels. Energy 2010;35:2511–6.

[29] Lorenzo E, Narvarte L, Muñoz J. Tracking and backtracking. Prog Photovolt, Res Appl 2011;19(6):747–53.

[30] Barbón A, Carreira-Fontao V, Bayón L, Silva CA. Optimal design and cost analysis of single-axis tracking photovoltaic power plants. Renew Energy 2023;211:626–46.

[31] Nascimento B, Albuquerque D, Lima M, Sousa P. Backtracking algorithm for single-axis solar trackers installed in a sloping field. Int J Eng Res Appl 2015;5(12):100–3.

[32] Anderson K. Maximizing yield with improved single-axis backtracking on cross-axis slopes. In: 2020 47th IEEE photovoltaic specialists conference. 2020, p. 1466–71.

[33] Anderson K, Mikofski M. Slope-aware backtracking for single-axis trackers (No. NREL/TP-5K00-76626). Golden, CO (United States): National Renewable Energy Lab.(NREL); 2020.

[34] Passow K, Lee K, Shah S, Fusaro D, Sharp J, Creasy L. Strategies to optimize and validate backtracking performance of single-axis trackers on sloped sites. In: Proc. IEEE 48th photovolt. spec. conf.. 2021, p. 1960–4.

[35] Leung M, Mikofski MA, Hamer M, Neubert A, Parikh A, Rainey P, et al. Tracker terrain loss part two. IEEE J Photovolt 12(1):127–32, 2121.

[36] Rhee K. Terrain aware backtracking via forward ray tracing. In: 2022 IEEE 49th photovoltaics specialists conference. 2022, p. 29–30.

[37] Duffie JA, Beckman WA. Solar engineering of thermal processes. John Wiley & Sons; 2013.

[38] Roth P, Georgiev A, Boudinov H. Cheap two axis sun following device. Energy Convers Manage 2005;46:1179–92.

[39] Casares de la Torre FJ, Varo M, López-Luque R, Ramírez-Faz J, Fernández-Ahumada LM. Design and analysis of a tracking / backtracking strategy for PV plants with horizontal trackers after their conversion to agrivoltaic plants. Renew Energy 2022;187:537–50.

[40] Makhdoomi S, Askarzadeh A. Impact of solar tracker and energy storage system on sizing of hybrid energy systems: A comparison between diesel/PV/PHS and diesel/PV/FC. Energy 2021;231:120920.

[41] Mamun MAA, Islam MM, Hasanuzzaman M, Selvaraj J. Effect of tilt angle on the performance and electrical parameters of a PV module: Comparative indoor and outdoor experimental investigation. Energy Built Environ 2022;3(3):278–90.

[42] Conceiçao R, Silva HG, Fialho L, Lopes FM, Collares-Pereira M. PV system design with the effect of soiling on the optimum tilt angle. Renew Energy 2019;133:787–96.

[43] Liu BYH, Jordan RC. The long-term average performance of flat-plate solar energy collectors. Sol Energy 1963;7:53–74.

[44] Hay JE, Davies JA. Calculation of the solar irradiance incident on an inclined surface. In: Hay JE, Won TK, editors. Proc. first Canadian solar radiation data workshop. Downsview, Ont.: Canadian Atmospheric Environment Service; 1980, p. 59–72.

[45] Perez R, Ineichen P, Seals R, Michalsky J, Stewart R. Modeling daylight availability and irradiance components from direct and global irradiance. Sol Energy 1990;44:271–89.

[46] Mehleri ED, Zervas PL, Sarimveis H, Palyvos JA, Markatos NC. Determination of the optimal tilt angle and orientation for solar photovoltaic arrays. Renew Energy 2010;35:2468–75.

[47] Koronakis PS. On the choice of angle of tilt for south facing solar collectors in Athens Basin Area. Sol Energy 1986;36:217–25.

[48] Badescu V. 3D isotropic approximation for solar diffuse irradiance on tilted surfaces. Renew Energy 2002;26:221–33.

[49] Tian YQ, Davies-Colley RJ, Gong P, Thorrold BW. Estimating solar radiation on slopes of arbitrary aspect. Agricult Forest Meteorol 2001;109:67–74.

[50] Bugler JW. The determination of hourly insolation on an inclined plane using a diffuse irradiance model based on hourly measured global horizontal insolation. Sol Energy 1977;19:477–91.

[51] Ma CCY, Iqbal M. Statistical comparison of models for estimating solar radiation on inclined surgaces. Sol Energy 1983;31:313–7.

[52] Iqbal M. An introduction to solar radiation. 1st ed.. Inc. New York: Academic Press; 1983.

[53] Temps RC, Coulson KL. Solar radiation incident upon slopes of different orientations. Sol Energy 1977;19:179–84.

[54] Klucher TM. Evaluation of models to predict insolation on tilted surfaces. Sol Energy 1979;23:111–4.

[55] Reindl DT, Beckman WA, Duffie JA. Diffuse fraction correlations. Sol Energy 1990;45:1–7.

[56] Jimenez JI, Castro-Díez Y. National Assembly of Geophysics and Geodesy II. 1986, p. 805.
[57] Barbón A, Bayón-Cueli C, Bayón L, Rodríguez-Suanzes C. Analysis of the tilt and azimuth angles of photovoltaic systems in non-ideal positions for urban applications. Appl Energy 2022;305:117802.
[58] Barbón A, Bayón-Cueli C, Bayón L, Carreira-Fontao V. A methodology for an optimal design of ground-mounted photovoltaic power plants. Appl Energy 2022;314(15):118881.
[59] Barbón A, Fortuny Ayuso P, Bayón L, Fernández-Rubiera JA. Predicting beam and diffuse horizontal irradiance using Fourier expansions. Renew Energy 2020;154:46–57.
[60] Joint Research Centre (JRC). Available from: http://re.jrc.ec.europa.eu/pvg_tools/en/tools.html#PVP. [Accessed on: 23 March 2023].
[61] Hottel HC. A simple model for estimating the transmittance of direct solar radiation through clear atmosphere. Sol Energy 1976;18:129–34.
[62] Liu BYH, Jordan RC. The interrelationship and characteristic distribution of direct, diffuse and total solar radiation. Solar Energy 1960;4:1–19.
[63] Kipp, Zonen. Available from: https://www.kippzonen.com/Products. [Accessed on: 23 March 2023].
[64] Al-Waeli AHA, Chaichan MT, Sopian K, Kazem HA, Mahood HB, Khadom AA. Modeling and experimental validation of a PVT system using nanofluid coolant and nano-PCM. Sol Energy 2019;177:178–91.
[65] Energy conversion for sustainable development, research group. 2023, Available from: https://www.unioviedo.es/bayon/ceds/index.html. [Accessed on: 23 March 2023].
[66] Baharuddin LSS, Rahim R. Daylight availability in Hong Kong: Classification into three sky conditions. Archit Sci Rev 2010;53:396–407.
[67] Kong HJ, Kim JT. A classification of real sky conditions for Yongin, Korea. Sustain Energy Build 2013;22:1025–32.